

# Iron and Nickel Line Diagnostics for the Galactic Center Diffuse Emission

Katsuji KOYAMA, Yoshiaki HYODO, Tatsuya INUI,

Hiroshi NAKAJIMA, Hironori MATSUMOTO, and Takeshi Go TSURU

*Department of Physics, Graduate School of Science, Kyoto University, Sakyo-ku, Kyoto 606-8502*

*koyama@cr.scphys.kyoto-u.ac.jp, hyodo@cr.scphys.kyoto-u.ac.jp*

Tadayuki TAKAHASHI, Yoshitomo MAEDA, and Noriko Y. YAMAZAKI

*Institute of Space and Astronautical Science, JAXA, 3-1-1 Yoshinodai, Sagamihara, Kanagawa 229-8510*

Hiroshi MURAKAMI

*PLAIN center, ISAS/JAXA, 3-1-1 Yoshinodai, Sagamihara, Kanagawa 229-8510*

Shigeo YAMAUCHI

*Faculty of Humanities and Social Sciences, Iwate University, 3-18-34 Ueda, Morioka, Iwate 020-8550*

Yohko TSUBOI

*Department of Physics, Faculty of Science and Engineering, Chuo University, 1-13-27 Kasuga, Bunkyo-ku, Tokyo 112-8551*

Atsushi SENDA

*The Institute of Physical and Chemical Research (RIKEN), 2-1 Hirosawa, Wako, Saitama 351-0198*

Jun KATAOKA

*Department of Physics, Tokyo Institute of Technology, Meguro-ku, Tokyo 152-8551*

Hiromitsu TAKAHASHI

*Department of Physical Science, School of Science, Hiroshima University, 1-3-1 Kagamiyama, Higashi-Hiroshima, Hiroshima 739-8526*

Stephen S. HOLT

*Olin College, Needham, MA 02492, USA*

and

Gregory V. BROWN

*High Energy Density Physics and Astrophysics Division, Lawrence Livermore National Laboratory, Livermore, CA 94551, USA*

(Received 2006 July 8; accepted 2006 August 16)

## Abstract

We have observed the diffuse X-ray emission from the Galactic Center (GC) using the X-ray Imaging Spectrometer (XIS) on Suzaku. The high-energy resolution and the low-background orbit provided excellent spectra of the GC diffuse X-rays (GCDX). The XIS found many emission lines in the GCDX near the energy of K-shell transitions of iron and nickel. The most pronounced features are Fe I  $K\alpha$  at 6.4 keV and K-shell absorption edge at 7.1 keV, which are from neutral and/or low ionization states of iron, and the K-shell lines at 6.7 keV and 6.9 keV from He-like (Fe XXV  $K\alpha$ ) and hydrogenic (Fe XXVI  $Ly\alpha$ ) ions of iron. In addition,  $K\alpha$  lines from neutral or low ionization nickel (Ni I  $K\alpha$ ) and He-like nickel (Ni XXVII  $K\alpha$ ), Fe I  $K\beta$ , Fe XXV  $K\beta$ , Fe XXVI  $Ly\beta$ , Fe XXV  $K\gamma$ , and Fe XXVI  $Ly\gamma$  were detected for the first time. The line center energies and widths of Fe XXV  $K\alpha$  and Fe XXVI  $Ly\alpha$  favor a collisional excitation plasma for the origin of the GCDX. The electron temperature determined from the line flux ratio of Fe XXV  $K\alpha$ /Fe XXV  $K\beta$  is similar to the ionization temperature determined from that of Fe XXV  $K\alpha$ /Fe XXVI  $Ly\alpha$ . Thus it would appear that the GCDX plasma is close to ionization equilibrium. The 6.7 keV flux and temperature distribution to the galactic longitude is smooth and monotonic, in contrast to the integrated point source flux distribution. These facts support the hypothesis that the GCDX is truly diffuse emission rather than the integration of the outputs of a large number of unresolved point sources. In addition, our results demonstrate that the chemical composition of Fe in the interstellar gas near the GC is constrained to be about 3.5 times solar abundance.

**Key words:** Galaxy: center — ISM: abundances — ISM: dust, extinction — X-ray spectra

## 1. Introduction

The iron K-shell lines near the Galactic Center (GCDX) was first detected with the Ginga satellite (Koyama et al. 1989; Yamauchi et al. 1990). The line energy is about 6.7 keV and the emission extends about  $1^\circ$ – $2^\circ$  over the Galactic Center (GC) region. The ASCA satellite observed more details of the GC region, and confirmed the nature of the GCDX (Koyama et al. 1996; Tanaka et al. 2000). Moreover, the ASCA CCD resolved the iron K-shell line detected with Ginga into three

distinct lines at 6.4, 6.7, and 6.9 keV (Koyama et al. 1996). The 6.7 and 6.9 keV lines are likely due to He-like (Fe XXV) and hydrogenic (Fe XXVI) ions of iron. There are three plausible scenarios that have been proposed for the origin of the iron K-shell lines. One is collisional excitation (CE) by low energy electrons, similar to the Galactic ridge emission. This process, however, contributes mainly to the 6.4 keV line emission, and not to the 6.7 and 6.9 keV lines (Valinia et al. 2000). With respect to the 6.7 keV and 6.9 keV lines, CE in a thin, high temperature plasma, and charge exchange (CX) recombination

**Table 1.** Suzaku on-source observations near the Galactic Center.

Target name	Sequence number	Pointing direction		Observation start	Effective exposure	
		$\alpha$ (J2000)	$\delta$ (J2000)		FI (ks)	BI (ks)
GC_SRC1	100027010	17 <sup>h</sup> 46 <sup>m</sup> 03 <sup>s</sup>	-28°55'32"	2005-09-23 07:07	48.6	48.3
GC_SRC2	100027020	17 <sup>h</sup> 45 <sup>m</sup> 13 <sup>s</sup>	-29°10'16"	2005-09-24 14:16	40.0	46.6
GC_SRC2	100037010	17 <sup>h</sup> 45 <sup>m</sup> 13 <sup>s</sup>	-29°10'16"	2005-09-29 04:25	47.6	47.7
GC_SRC1	100037040	17 <sup>h</sup> 46 <sup>m</sup> 03 <sup>s</sup>	-28°55'32"	2005-09-30 07:41	47.1	47.1

are both considered. For the CE case, the best-fit thin thermal plasma temperature of the GCDX spectrum was  $\sim 10$  keV. If the GCDX is really due to a thin hot and uniformly distributed plasma, the total thermal energy is estimated to be  $10^{53-54}$  erg, or equivalent to  $10^2-10^3$  supernovae explosions. The temperature of  $\sim 10$  keV is higher than that bounded by the Galactic gravity, hence the plasma should escape from the GC region. The time scale estimated by the plasma size ( $1^\circ$  or  $\sim 150$  pc at 8.5 kpc) divided by the sound velocity of the  $\sim 10$  keV plasma is  $\sim 10^5$  years. Therefore the energy of  $\sim 10^{53-54}$  erg should be supplied in the past  $\sim 10^5$  years, e.g. 1 SN every 100–1000 years is required in the GC region. This huge energy budget in the GC region suggests that CX recombination may be a more reasonable explanation for the GCDX. In this scenario, during a collision between neutral hydrogen and Fe XXVI or Fe XXVII, the bound hydrogen electron is captured into an excited state of the iron, and then the excited state decays producing an X-ray. The X-ray spectral signature is distinct from the signature produced by CE in a collisional ionization equilibrium (CIE) plasma, such as the high-temperature plasma mentioned above. In the CX case, the forbidden line at  $E_f = 6636$  eV, is stronger than the resonance line at  $E_r = 6700$  eV (Otranto et al. 2006; Beiersdorfer et al. 2005; Wargelin et al. 2005), whereas the resonance line is stronger in the case of a plasma in CIE. Thus, even if the resonance and forbidden lines are not completely resolved, the energy centroid of the  $K\alpha$  line of Fe XXV produced by CX will be lower than that produced by CE. We also note that an energy shift towards lower energy as the CX would be observed in the case of X-ray emission following recombination with low energy electrons, as in a photo-ionized plasma (Beiersdorfer 2003).

The 6.4 keV line is likely to be  $K\alpha$  from the neutral and/or a blend of low charge states of iron (here, Fe I). In fact, the 6.4 keV line is localized near molecular clouds such as the radio complex Sgr B2 and the Radio Arc regions. Sgr B2, the most massive giant molecular cloud with ultra compact H II and many maser sources, has been extensively studied with ASCA and Chandra (Koyama et al. 1996; Murakami et al. 2000, 2001). As a result of those studies, the authors proposed that the 6.4 keV line arose in an X-ray reflection nebula irradiated by Sgr A\* during an exceptionally bright period that occurred about 300 years ago, i.e., a time span equivalent to the light traveling time between Sgr B2 and Sgr A\*. This putative high activity of Sgr A\* could provide the energy supply to the GCDX.

Accordingly, a high quality observation of the iron and nickel K-shell lines can provide key information for understanding the origin of the GCDX. Using the X-ray Imaging

Spectrometer (XIS) (Koyama et al. 2007a), we have measured X-ray emission for the spectral band containing these lines. The XIS is the X-ray CCD camera system on board Suzaku (Mitsuda et al. 2007). The excellent energy resolution and well-calibrated performance for diffuse sources, coupled with the low background orbit of Suzaku, make the XIS well-suited to provide crucial information about the GCDX. Here we present the results of the first measurement of the GCDX with the XIS focusing on the K-shell emission from iron and nickel.

## 2. Observations and Data Processing

Two pointing observations towards the GC were performed with the XIS at the focal planes of the X-Ray Telescope (XRT) on board the Suzaku satellite in September of 2005. Details of Suzaku, the XRT, and the XIS are found in Mitsuda et al. (2007), Serlemitsos et al. (2007), and Koyama et al. (2007a), respectively. Data taken at elevation angles less than  $5^\circ$  from the Earth rim or during the passage through the South Atlantic Anomaly were discarded. After this filtering, the net exposure times were  $\sim 180$  ks and  $\sim 190$  ks for the front-illuminated (FI) CCDs and the back-illuminated (BI) CCD, respectively. The observation logs are listed in table 1.

Since the GCDX extends beyond the field of view (FOV) of the XIS, the strong K-shell lines were found in the full imaging area of the XIS CCD. We therefore made a fine correction of the charge transfer inefficiency (CTI) and fine gain tuning of CCD-to-CCD and segment-to-segment levels (for the CTI and the CCD segment, see Koyama et al. 2007a). These fine tunings were done using the  $K\alpha$  lines of Fe XXV (6.7 keV), Fe I (6.4 keV), and helium-like silicon (S XV) (2.46 keV). The absolute gain tuning was made using the  $^{55}\text{Fe}$  calibration sources irradiating the CCD corners. Details of the fine tuning are given in the Appendix.

## 3. Analysis and Results

### 3.1. The Image and Spectrum near the Iron and Nickel K-Line Complexes

After the CTI-correction and the fine gain-tuning, we co-added the four XIS data sets and made X-ray mosaic maps of the GC region. Figures 1 and 2 show the narrow band maps in the 6.34–6.46 keV and 6.62–6.74 keV bands, where the vignetting correction was applied. These represent the  $K\alpha$  lines of Fe I and Fe XXV. The sharp contrast in these two adjacent lines demonstrates that the GCDX exhibits a large variety in different emission lines.

We made the X-ray spectrum from the whole region of

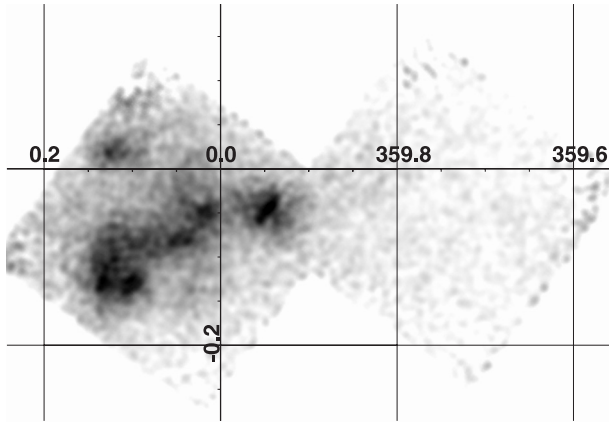


**Fig. 1.** The narrow band map at the 6.4 keV line (the 6.34–6.46 keV band). Coordinates are galactic  $l$  and  $b$  in degrees.

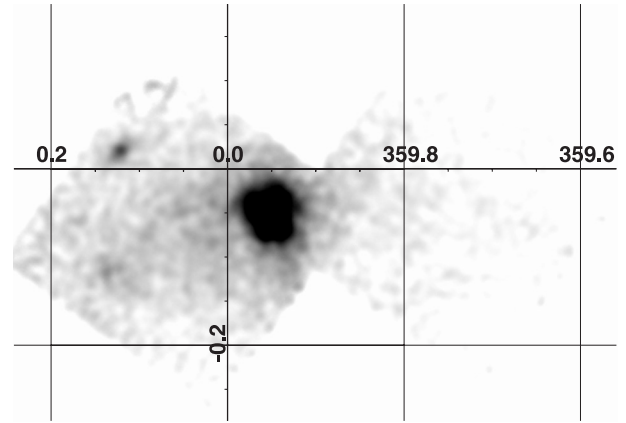


**Fig. 2.** Same as figure 1, but for the 6.7 keV line (the 6.62–6.74 keV band).

figures 1 and 2 excluding the corners of the CCD, containing the calibration sources and the central bright object Sgr A East (Maeda et al. 2002; Sakano et al. 2004; Park et al. 2005; Koyama et al. 2007b). Since the relative gain of each XIS set and segment is well calibrated (see Appendix), and the response functions for each XIS set are essentially the same, we added the spectra of the three front-illuminated (FI) CCDs (XIS 0, 2, and 3) to increase photon statistics. To estimate the NXBG, we used the night Earth data accumulated by the XIS team (Koyama et al. 2007a). The data were sorted with the geomagnetic cut-off rigidity (COR), hence we compiled the data set such that the COR distribution became the same as that of the source observation. In reality, the NXBG flux sorted with the COR differs by less than 3% from that without sorting. In the NXBG subtraction, we adjusted the pulse height of the calibration sources and instrumental lines (see Koyama et al. 2007a) in the NXBG data to those of the GCDX. The NXBG-subtracted spectrum of the three FI CCDs is given in figure 3. The back-illuminated (BI) CCD spectrum was constructed in the same manner.

We can see many line structures in the 6–9 keV band as well as an apparently featureless continuum emission in the 9–11.5 keV band. In order to obtain the center energy, flux, and width of each line, we simultaneously fitted the spectra from the three FI CCDs and the BI CCD spanning the 5.5–11.5 keV band. The model used here is bremsstrahlung absorbed by  $N_{\text{Fe}}$  for the continuum, adding Gaussian profiles for emission lines. In the case of a line blend without sufficient counts to unambiguously resolve all the components, we fixed the energies of weaker lines relative to the stronger lines, referring the atomic data from Kaastra and Mewe (1993). For example, the line energy of Fe I  $K\beta$  was fixed to  $1.103 \times E(\text{Fe I } K\alpha)$ , that of Fe XXV  $K\beta$  was  $E(\text{Ni XXVII } K\alpha) + 110 \text{ eV}$ , and that of Fe XXV  $K\gamma$  was  $E(\text{Fe XXVI } \text{Ly}\beta) + 44 \text{ eV}$ . As for the widths of weak lines, they were either fixed to 30 eV (see next section) or fixed to the likely values referring to the related lines (see table 2). The best-fit model is given in figure 3, while the best-fit parameters are given in table 2.

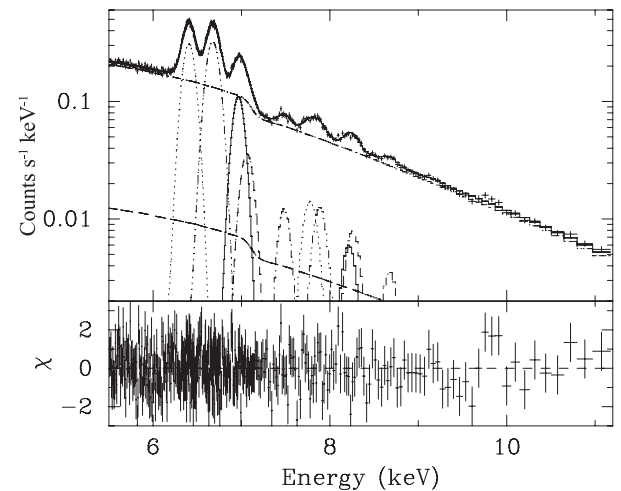


**Fig. 3.** The averaged spectrum of the 3 FI CCDs in the 5.5–11.5 keV band. The data are taken from the full FOV excluding the calibration source regions and Sgr A East. The spectra of the three FIs and BI are simultaneously fitted with a model of a thermal bremsstrahlung plus ten Gaussian lines and an iron absorption edge. The best-fit result of the three-FI spectrum is only shown. The long-dashed line is the model of the cosmic X-ray background (CXB).

### 3.2. The Reliability of the Center Energy and Width of the Emission Lines

Since the Fe XXVI  $\text{Ly}\alpha$  line has a relatively simple structure, its centroid can be accurately predicted. In the case of our measurement, the line flux was strong enough to determine the centroid energy with high accuracy. The theoretically predicted and observed centroids are 6966 eV and  $6969^{+6}_{-3} \text{ eV}$  (errors in this paper are at 90% confidence level unless otherwise mentioned). Also the calibration energies of the characteristic  $K\alpha$  and  $K\beta$  lines from neutral Mn (Mn I) agree with the theoretical energy within 1 eV. These agreements demonstrate that our procedure of the CTI correction and fine gain-tuning worked well. Since the error on the center energy of Fe XXVI  $\text{Ly}\alpha$  is  $^{+6}_{-3} \text{ eV}$ , we regard the overall systematic error

**Table 2.** The best-fit parameters of the GCDX.\*

Continuum				
$N_{\text{H}}$ (cm <sup>-2</sup> )	$6 \times 10^{22}$ (fixed)			
$N_{\text{Fe}}$ (cm <sup>-2</sup> )	$9.7^{+0.7}_{-0.4} \times 10^{18}$			
$kT_e$ (keV)	$15^{+2}_{-1}$			
Emission lines				
Center energy (eV)	Identification Line	Energy (eV) <sup>†</sup>	Width <sup>‡</sup> (eV)	Intensity (photons s <sup>-1</sup> cm <sup>-2</sup> )
$6409 \pm 1$	Fe I <sup>  </sup> K $\alpha$		$33^{+2}_{-4}$	$4.32^{+0.05}_{-0.08} \times 10^{-4}$
$6680 \pm 1$	Fe XXV K $\alpha$	6637–6701	$39 \pm 2$	$5.10^{+0.08}_{-0.06} \times 10^{-4}$
$6969^{+6}_{-3}$	Fe XXVI Ly $\alpha$	6966	$15^{+8}_{-15}$	$1.66^{+0.09}_{-0.11} \times 10^{-4}$
$7069^{\S}$	Fe I <sup>  </sup> K $\beta$		$38^{\#}$	$6.91^{+1.12}_{-0.96} \times 10^{-5}$
$7490^{+12}_{-14}$	Ni I <sup>  </sup> K $\alpha$		$0 (< 28)$	$3.05^{+0.73}_{-0.57} \times 10^{-5}$
$7781^{+24}_{-31}$	Ni XXVII K $\alpha$	7735–7805	$39^{**}$	$3.97^{+1.06}_{-0.65} \times 10^{-5}$
$7891^{\dagger\dagger}$	Fe XXV K $\beta$	7881	30 (fixed)	$4.69^{+0.81}_{-0.61} \times 10^{-5}$
$8220^{+31}_{-22}$	Fe XXVI Ly $\beta$	8251	30 (fixed)	$2.29^{+1.35}_{-1.31} \times 10^{-5}$
$8264^{\dagger\dagger}$	Fe XXV K $\gamma$	8295	30 (fixed)	$3.08^{+1.32}_{-1.34} \times 10^{-5}$
$8681^{+33}_{-32}$	Fe XXVI Ly $\gamma$	8700	$0 (< 91)$	$1.77^{+0.62}_{-0.56} \times 10^{-5}$
Calibration source line				
$5896^{+1}_{-1}$	Mn I K $\alpha$	5895	$31^{+1}_{-1}$	
$6489^{+1}_{-2}$	Mn I K $\beta$	6490	$38^{+1}_{-3}$	

\* The errors are at 90% confidence level.

<sup>†</sup> Chandra ATOMDB1.3<sup>1</sup> and Wargelin et al. (2005).<sup>‡</sup> One standard deviation ( $1\sigma$ ).<sup>§</sup> Fixed to  $1.103 \times E(\text{Fe I K}\alpha)$ .<sup>||</sup> Neutral or low ionization state.<sup>#</sup> Fixed to  $1.103 \times \sigma(\text{Fe I K}\alpha)$ .<sup>\*\*</sup> Fixed to  $\sigma(\text{Fe XXV K}\alpha)$ .<sup>††</sup> Fixed to  $110 + E(\text{Ni XXVII K}\alpha)$ .<sup>†††</sup> Fixed to  $44 + E(\text{Fe XXVI Ly}\beta)$ .

of our gain determination in the iron energy band to be within  $^{+3}_{-6}$  eV.

The observed line widths (after the de-convolution of the response function) of Mn I K $\alpha$  and Fe I K $\alpha$  are  $31 \pm 1$  eV and  $33^{+2}_{-4}$  eV ( $1\sigma$ ), respectively. The energy resolution has been gradually decreasing since the launch in 2005 July, and the line broadening is consistent with the long-term CCD degradation for the calibration line. The time dependent energy resolution is currently not well-enough understood to implement here, but it is important to note that the observations reported here were made early in the mission. The apparent line broadening (here, the systematic broadening) of  $\sim 30$  eV at  $\sim 6$ – $7$  keV is mainly due to the long-term degradation of the CCD energy resolution, since, as described below, there are internal consistencies that argue against other systematic causes. (1) The calibration line (<sup>55</sup>Fe) is irradiating a small spot of the CCD, therefore any line broadening due to non-uniformity of the gain and non-linearity of the CTI (if any) in the CCD area can be ignored for the calibration line. (2) Because the 33 eV line broadening of the 6.4 keV line in the GCDX spectrum agrees with the broadening of the calibration line (31 eV at 5.9 keV),

it follows that the source of the broadening is the same for both the calibration and the GCDX line feature. (3) The observed line broadening for the 6.9 keV line is less than the calibration line (see discussion below), hence no line broadening is found in the 6.9 keV line, (4) We divided the observations into two terms (Sequence numbers 100027010+100027020 and 100037010+100037040, see table 1) separated by about one week and examined the center energies. The observed difference of the center energy of Fe XXV K $\alpha$  is only 1 eV, well within the statistical error of 1 eV. Therefore the gain was almost constant in the observational period, hence did not cause any line broadening in the integrated spectrum.

Apart from the line broadening caused by the long-term degradation of the CCDs, we can safely conclude that the response function is well-calibrated for the present observation, especially for the line center energy.

## 4. Discussion

### 4.1. Over Abundance of Fe in the Interstellar Gas

The continuum shape of the GCDX spectrum is well reproduced with the addition of an Fe K-edge at 7.1 keV. The best-fit column density,  $N_{\text{Fe}}$ , is determined to be  $9.7^{+0.7}_{-0.4} \times 10^{18}$  cm<sup>-2</sup>.

<sup>1</sup> <http://cxc.harvard.edu/atomdb/WebGUIDE/index.html>.

This corresponds to an iron abundance of 3.5 times solar assuming a typical hydrogen column density ( $N_{\text{H}}$ ) toward the GC of  $6 \times 10^{22} \text{ cm}^{-2}$  (Sakano et al. 2002) and the solar abundances of Anders and Grevesse (1989). We expect that a large fraction of this absorption takes place in the dense gas clouds prevailing near the GC region.

#### 4.2. $K\alpha$ Line from Fe I

The energy of Fe I  $K\alpha$  is 6400 eV (Kaastra, Mewe 1993), which is lower than that found in the GCDX of  $6409 \pm 1 \text{ eV}$  by 9 eV. However, because the energy difference of 9 eV is larger than the systematic error of  ${}_{-6}^{+3} \text{ eV}$ , we suspect that this difference is a result of blending of Fe I  $K\alpha$  with line emission from low charge states of iron. The line width of  $33_{-4}^{+2} \text{ eV}$  is comparable to, but slightly larger than, the systematic broadening of  $\sim 30 \text{ eV}$ , which may also be the result of the line blending.

#### 4.3. $K\alpha$ Line from Fe XXVI

The line width of Fe XXVI  $K\alpha$  is determined to be  $\leq 23 \text{ eV}$ , which is smaller than the systematic broadening of  $\sim 30 \text{ eV}$ . This unnaturally narrow line could be due to the coupling with the nearby line Fe I  $K\beta$ . We therefore examined the coupling effect by fixing to the theoretically predicted flux of  $0.125 \times K\alpha$  (Kaastra, Mewe 1993). The best-fit result of  $25_{-8}^{+5} \text{ eV}$  is consistent with the systematic broadening. Thus we can safely conclude that the line width broadening of Fe XXVI  $K\alpha$  is instrumental.

#### 4.4. The Center Energy and Width of Fe XXV $K\alpha$

The Fe XXV  $K\alpha$  line is a blend of the resonance, intercombination, and forbidden lines from Fe XXV (see table 3), and depending on the conditions of the source plasma, may also contain satellite lines produced by dielectronic recombination and innershell excitation (Beiersdorfer et al. 1992, 1993). The fact that the observed line centroid and width of Fe XXV  $K\alpha$  depends on the flux ratio of these lines, which, in turn, are a function of the plasma conditions, make the  $K\alpha$  line feature an excellent diagnostic. As discussed above, a centroid shifted towards lower energy relative to the CIE case is an indication of a recombining plasma. For the GCDX, the observed center energy of Fe XXV  $K\alpha$  is  $6680 \pm 1 \text{ eV}$ . We compared our result to the laboratory values produced by the CX recombination, i.e., a recombination dominated plasma, and also to calculations using APEC and MEKAL of the line emission produced by a CIE plasma. The laboratory measured line centroid of Fe XXV  $K\alpha$  produced by the CX recombination alone, is  $6666 \pm 5 \text{ eV}$  (Wargelin et al. 2005), significantly lower than the value measure in the GCDX. The APEC and MEKAL predicted centroids for the CIE case are 6685 eV and 6680 eV, respectively, in agreement with the GCDX value of 6680 eV.

We also note that the line broadening of  $39 \pm 2 \text{ eV}$  for Fe XXV  $K\alpha$  is larger than the systematic broadening of  $\sim 30 \text{ eV}$  (see subsection 3.2). This must be due to the fact that several lines contribute to this line feature.

#### 4.5. Constraints on the Cosmic Ray Iron Velocity in Charge Exchange Scenario

The relatively high resolution of the XIS also affords us the ability to extract crucial information from the line feature

**Table 3.** He-like iron triplets.

Name	Transition	Energy (eV)*
Resonance	$1s^2 \ ^1S_0 - 1s \ 2p \ ^1P_1$	6701
Intercombination	$1s^2 \ ^1S_0 - 1s \ 2p \ ^3P_1$	6682
Intercombination	$1s^2 \ ^1S_0 - 1s \ 2p \ ^3P_2$	6668
Forbidden	$1s^2 \ ^1S_0 - 1s \ 2p \ ^3S_1$	6637

\* From Wargelin et al. (2005).

of Fe XXVI  $\text{Ly}\alpha$ , which provides further evidence against the CX process for X-ray production. As discussed in subsection 4.3, the intrinsic line broadening of  $\text{Ly}\alpha$  is nearly zero, and it follows that if CX is the source of the X-ray emission, then recombination would occur when the bare iron velocity is nearly zero, i.e., the collision energy between the iron ion and neutral hydrogen is small. In such a low-collision energy case, electrons are non-statistically captured into levels with large principal quantum numbers ( $n \geq 10$ ) (Wargelin et al. 2005; Perez et al. 2001; Otranto et al. 2006). We, however, see no enhancement at the Fe XXVI Rydberg series limit at 9.2 keV. Our measurements give an upper limit of  $9 \times 10^{-6} \text{ photons s}^{-1} \text{ cm}^{-2}$  for the high- $n$  Rydberg series line emission (we assumed a Gaussian line with width of 30 eV), only about 6% of the intensity of  $\text{Ly}\alpha$ . This upper limit corresponds to a lower limit of collision energy of  $100 \text{ eV amu}^{-1}$  (Perez et al. 2001; Wargelin et al. 2005) between bare Fe nuclei and neutral H. For that collision energy, the velocity of bare iron nuclei must be larger than  $\sim 150 \text{ km s}^{-1}$ . Therefore the CX process, if present in the GCDX, gives a lower limit on the velocity of  $\sim 150 \text{ km s}^{-1}$ . Tanaka (2002) suggested that the CX process may have the maximum cross section at a higher iron velocity of  $\sim 5000 \text{ km s}^{-1}$ , hence the subsequent decay lines have widths of about 100 eV. No such large broadening was observed in Fe XXVI  $\text{Ly}\alpha$ .

Together with the discussion of subsection 4.4, we therefore propose that the 6.7 keV and 6.9 keV lines in the GCDX are likely due to a CIE plasma and would not arise from a CX process.

#### 4.6. The Flux Ratio of K-Shell Transition Lines from Fe XXV, XXVI, and Ni XXVII

The K-shell lines of Fe XXV  $K\alpha$  and Fe XXVI  $\text{Ly}\alpha$  were discovered with the data from ASCA (Koyama et al. 1996), Chandra (Muno et al. 2004), and XMM-Newton (Predehl et al. 2003). With Suzaku, we have, for the first time, detected Ni XXVII  $K\alpha$ , Fe XXV  $K\beta$ , and Fe XXVI  $\text{Ly}\beta$ . We have also tentatively identified Fe XXV  $K\gamma$  and Fe XXVI  $\text{Ly}\gamma$  (see table 2). As discussed in subsections 4.4 and 4.5, the emission lines from these highly ionized atoms are likely due to collisional excitation in a thin thermal plasma. The best-fit flux ratio of Fe XXVI  $\text{Ly}\alpha/\text{Fe XXV } K\alpha$  is  $0.33 \pm 0.02$ , which provides an ionization temperature of  $6.4 \pm 0.2 \text{ keV}$ . The best-fit flux ratio of Fe XXV  $K\beta/\text{Fe XXV } K\alpha$  is  $0.092_{-0.012}^{+0.016}$ , which gives the electron temperature of  $6.6_{-1.7}^{+4.2} \text{ keV}$ . Although the error is still large, this electron temperature is similar to the ionization temperature. The line flux ratio of Ni XXVII  $K\alpha/\text{Fe XXV } K\alpha$  is 0.078. With the further assumption that the relative

abundances of iron and nickel are proportional to the solar value, this ratio is converted to the plasma temperature of  $\sim 5.4$  keV. We therefore conclude that the GCDX plasma has a temperature of  $\sim 5\text{--}7$  keV in collisional ionization equilibrium. The observed flux ratios of Fe XXVI Ly $\beta$ /Fe XXVI Ly $\alpha$ , Fe XXV K $\gamma$ /Fe XXV K $\alpha$ , and Fe XXVI Ly $\gamma$ /Fe XXVI Ly $\alpha$  are consistent with this plasma condition.

#### 4.7. Temperature and Flux Variations of the GCDX Plasma

Although we show that the GCDX is attributable to a high temperature plasma of  $\sim 5\text{--}7$  keV in collisional ionization equilibrium, whether the origin is diffuse or the integrated emission of a large number of unresolved point sources, is not yet clear. We therefore investigated the spatial variation of the GCDX in temperature and flux. We made a series of X-ray spectra in  $3' \times 6'$  rectangles along the Galactic plane of  $b = -0^\circ.05$  (figure 4), then extracted the fluxes of the 6.7 and 6.9 keV lines, applying the same model as is given in table 2. The plots of the flux ratio between the 6.7 and 6.9 keV lines, and the fluxes of the 6.7 keV line are given in figure 5 and figure 6, respectively, in which the flux and flux ratio of the bright SNR Sgr A East are excluded. We see that the 6.7 and 6.9 keV line ratio is constant at  $\sim 0.38$  in the negative longitude region from  $l = -0^\circ.1$  to  $l = -0^\circ.4$ , but decreases to  $\sim 0.30$  at the positive longitude near at  $l = 0^\circ.25$ . The ratios of 0.38 and 0.30 suggest ionization temperatures of 6.8 keV and 6.2 keV, respectively. The smooth and monotonic variation of the ionization temperature along the galactic longitude argues that the GCDX is not due to the superposition of the outputs of a large number of unresolved point sources.

We simulated the point-source flux in the 4.7–8.0 keV band observed with the XIS, putting the positions and fluxes (2.0–8.0 keV band) of the Chandra cataloged sources (Muno et al. 2003) in the same rectangles of figure 4. To preserve completeness limit, we selected the sources with flux larger than  $5 \times 10^{-7}$  photons  $\text{cm}^{-2} \text{s}^{-1}$  in the 2.0–8.0 keV band. After convolving the response of the XRT+XIS, we extracted the integrated point-source fluxes from each rectangle. The results are plotted in the same figure of the 6.7 keV line (figure 6). The integrated point-source flux is symmetrically distributed between positive and negative galactic longitude with a sharp peak at Sgr A\* ( $l = -0^\circ.06$ ), which is significantly different from the 6.7 keV line flux distribution. The 6.7 keV line flux shows an asymmetric distribution (larger flux at the positive galactic longitude than the negative side) and a gradual increase towards Sgr A\*. These facts suggest that the major fraction of the 6.7 keV line flux is not due to the integrated emission of unresolved point sources, but is truly diffuse.

#### 4.8. Hard X-Ray Tail

From the line diagnostics, the GCDX is most likely produced by a thin hot plasma with a temperature of  $\sim 5\text{--}7$  keV in CIE, while the bremsstrahlung temperature determined with the continuum shape in the 5.5–11.5 keV band is  $\sim 15$  keV (see table 2), significantly higher than  $\sim 5\text{--}7$  keV. This suggests that the continuum flux may contain an additional hard component. We therefore fitted the spectrum with a model of a CIE plasma and power-law component with 3 Gaussian lines for the K-shell emissions from Fe I and Ni I. In this model, the K-edge

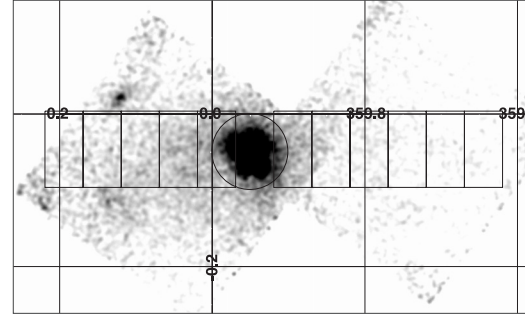


**Fig. 4.** Image of the 2 fields of view (FOV) in the 6.62–6.74 keV band, overlaid with the rectangular regions from which the spectra were extracted.

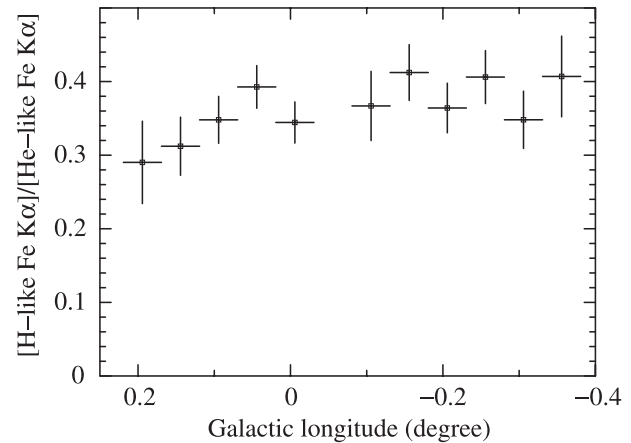


**Fig. 5.** The line flux ratios of Fe XXVI Ly $\alpha$ /Fe XXV K $\alpha$  measured in the series of rectangular regions along the Galactic plane given in figure 4 (the constant  $b = -0^\circ.05$  line).

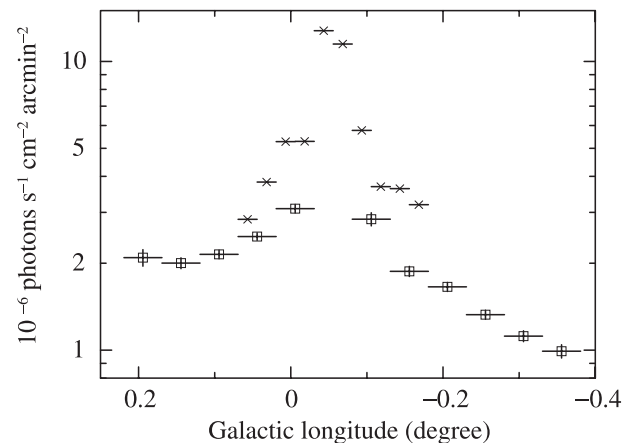


**Fig. 6.** The line fluxes of Fe XXV K $\alpha$  are given by the squares, while the integrated point source fluxes in the 4.7–8 keV band are plotted by the crosses. The horizontal axis is the same as figure 5, but the vertical axis is a logarithmic scale.

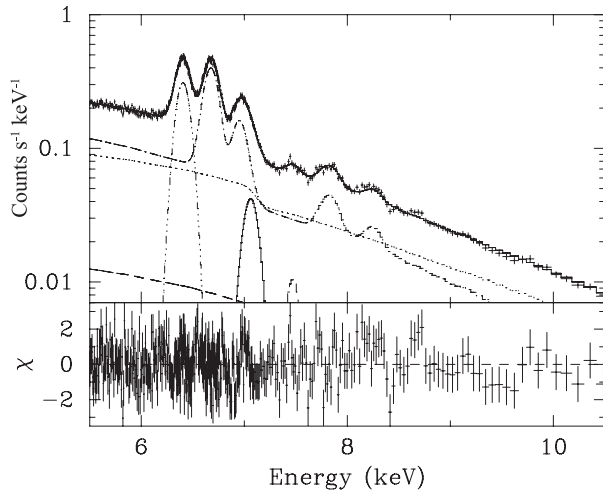
absorption with  $N_{\text{Fe}}$  is also implemented. Although its contribution is minor, we added the model spectrum of the cosmic X-ray background (CXB). As discussed in subsection 3.2, there are systematic errors in the line width ( $\sim 30$  eV) and

**Table 4.** Best-fit parameter with the VAPEC model.

Parameter	Unit	Value	
$N_{\text{H}}$	$\text{cm}^{-2}$	$6 \times 10^{22}$ (fixed)	
$N_{\text{Fe}}$	$\text{cm}^{-2}$	$8.5^{+0.8}_{-0.5} \times 10^{18}$	
$kT_e$	keV	$6.5^{+0.1}_{-0.1}$	
$Z_{\text{Fe}}$	solar	$1.2^{+0.5}_{-0.3}$	
$Z_{\text{Ni}}$	solar	$2.1^{+0.7}_{-0.5}$	
Velocity	$\text{kms}^{-1}$	1192	
Redshift		$6.0 \times 10^{-4}$	
Hard tail			
$\Gamma$		$1.4^{+0.5}_{-0.7}$	
Flux at 8 keV	$\text{photons s}^{-1} \text{cm}^{-2} \text{keV}^{-1}$	$4.5^{+1.9}_{-2.1} \times 10^{-4}$	
Emission lines			
Center energy (eV)	Identification Line Energy (eV)	Width (eV)	Intensity ( $\text{photons s}^{-1} \text{cm}^{-2}$ )
$6409^{+1}_{-1}$	Fe I <sup>†</sup> K $\alpha$	$36^{+1}_{-3}$	$4.41^{+0.05}_{-0.08} \times 10^{-4}$
7069.1*	Fe I <sup>†</sup> K $\beta$	39*	$7.8^{+0.4}_{-0.6} \times 10^{-5}$
$7492^{+14}_{-18}$	Ni I <sup>†</sup> K $\alpha$	0 (< 30)	$2.3^{+0.7}_{-0.4} \times 10^{-5}$

\* Fixed to  $1.103 \times E$  (Fe XXV K $\alpha$ ).

† Or low ionization state.

**Fig. 7.** Same as figure 3, but the model is a CIE plus a power-law with 3 Gaussian lines and an iron absorption edge.

center energy ( $^{+3}_{-6}$  eV). We therefore introduced an artificial random motion and small red-shift to cancel these systematic errors. The fit is reasonably good and the best-fit results and parameters are given in figure 7 and table 4. We note that the forbidden line of Ni XVII and some of the satellite lines are missing in the APEC model, hence the Ni abundance may be overestimated.

One notable finding is the presence of power-law hard tail. The power-law index  $\Gamma$  is sensitive to the slope of the high energy continuum. Because the effective area of the XRT–XIS combination drops rapidly at high energy, our determination of

the power-law index  $\Gamma$  has a relatively large statistical error of  $\Gamma \sim 1.4^{+0.5}_{-0.7}$ . The low numbers of counts make it challenging to determine the error contribution from systematic effects. To provide a more reliable estimate of the systematic error, we checked it using the spectrum of the Crab nebula. We examined the variation of the best-fit  $\Gamma$  by fitting the Crab spectrum in the 4–10, 5–10, 6–10, and 7–10 keV bands, and found no systematic variations with the increasing energy band. The mean variations of  $\Gamma$  are within 5% for all the XIS sets, which is far smaller than the statistical error of  $\sim 40\%$ .

Since the flux level of the NXBG becomes comparable to the hard tail flux at 8–10 keV, it may be argued that the error due to the NXBG-subtraction should not be ignored. The possible flux error of the NXBG is estimated to be  $\sim \pm 3\%$  (Koyama et al. 2007a). Including this error in the spectrum, the best-fit  $\Gamma$  are 1.4 (adding 3% of the NXBG) and 1.2 (3% reduction of the NXBG). Further systematic analysis of the NXBG found a hint that the flux of the night Earth data is smaller than that from a blank sky. The details of the flux difference is still in study, but is at a level of  $\leq 10\%$  at the 8–11 keV band. If we use a NXBG of  $1.1\times$  of the night Earth, then the best-fit  $\Gamma$  becomes 1.5. Thus any possible systematic error of NXBG does not change the conclusion that a flat hard tail is present in the GCDX. In addition, the flux of the CXB is more than one order of magnitude smaller than the hard tail in the hard X-ray band, so that the fluctuation and/or error of the CXB can be ignored.

A possible contributor of the power-law hard tail is non-thermal filament structures found with Chandra (Morris et al. 2003; Senda et al. 2002; Park et al. 2004). In fact, the power-law flux in the positive galactic longitude (GC\_SRC1) is significantly larger than that of the negative galactic longitude

(GC\_SRC2), which is a trend similar to the population of the non-thermal filaments (Morris et al. 2003; Senda et al. 2002; Park et al. 2004). The origin of the non-thermal emission is a key for understanding the presence of high energy particles, which are suggested by the detection of very high energy Gamma-rays (Aharonian et al. 2006; Tsuchiya et al. 2004; Kosack et al. 2004). Further analysis of the XIS data in combination with those of the Hard X-ray Detector (HXD) (Takahashi et al. 2007) could yield an important contribution to the study of this hard component.

## 5. Summary

1. Since the difference between the theoretical (6966 eV) and observed ( $6969_{-3}^{+6}$  eV) values of Fe XXVI Ly $\alpha$  is only 3 eV, we can assume that the detector gain and uniformity are well-calibrated to study features at this level of accuracy.
2. The abundance of Fe in the interstellar gas near the GC appears to be 3.5 times solar.
3. The 6.4 keV ( $K\alpha$  of neutral iron) line from the GC region could be contaminated by those of low ionization states, but still characteristic of gas at temperature much lower than those in which the helium-like lines arise.
4. The observed line centroid energy of Fe XXV  $K\alpha$  is  $6680 \pm 1$  eV, which is consistent with that of the collisional ionization plasma.
5. The GCDX spectrum is consistent with that of a CIE plasma with mean temperature 5–7 keV.
6. The plasma temperature of GXDX is constant at 6.8 keV in the galactic longitude region from  $l = -0.^\circ 1$  to  $l = -0.^\circ 4$ , while exhibiting a significant decrease to 6.2 keV near  $l = +0.^\circ 25$ .
7. The flux distribution of the 6.7 keV line along the Galactic plane is different from that of the integrated point sources.
8. We found a clear hard tail in the GCDX.

The authors express sincere thanks to all the Suzaku team members, especially A. Bamba, H. Uchiyama, H. Yamaguchi, and H. Mori for their comments and supports. Y.H. and H.N. are supported by JSPS Research Fellowship for Young Scientists. This work is supported by the Grants-in-Aid for the 21st Century COE “Center for Diversity and Universality in Physics” and also by Grants-in-Aid (No. 18204015) of the Ministry of Education, Culture, Sports, Science and Technology (MEXT). Work by UC LLNL was performed under the auspices of the U.S. Department of Energy by University of California, Lawrence Livermore National Laboratory under Contract W-7405-Eng-48.

## Appendix. The Internal Calibration of CTI and Gain Tuning

Since the GCDX emits strong lines covering over the entire field view of the XIS, we can calibrate the gain and its variation in the full XIS imaging area (IA). For this purpose, we divided each XIS set area into 4 sections along the *ACTY*-axis and designate them as No.1 to 4 in the order of the distance from the signal read-out nodes (No.4 corresponds to the largest *ACTY*, while No.1 is the smallest). The definition of *ACTY* is given in Koyama et al. (2007a). Figures 8, 9, and 10 are the plots of the line center energy of S XV  $K\alpha$ , Fe I  $K\alpha$ , and Fe XXV  $K\alpha$ , respectively.

From figures 8, 9, and 10, we see a clear trend that the line center energy is lower at longer distance from the read-out nodes. The effect is clearly instrumental (rather than astronomical), since the trend is observed in all four XIS detectors, with differing read-out orientations on the sky (Koyama et al. 2007a). Therefore, we can safely conclude that the systematic trend that the center energy decreases as increasing *ACTY* is due to the charge transfer inefficiency (CTI). Assuming that CTI is a linear function of the distance from the read-out nodes, we corrected the CTI so that the center energies of the three  $K\alpha$  lines become constant along the *ACTY* axis.

The CTI-corrected plots are given in figures 11, 12, and 13. The systematic decreases of the center energy along the *ACTY*-axis disappear, demonstrating that the CTI correction is properly made. We should note that the CTI at 6.4 and 6.7 keV is consistent with that at 5.9 keV from the calibration sources reported by the XIS team (Koyama et al. 2007a). Note also that we have corrected the CTI for each XIS set independently, but the CTI is assumed to be identical in the 4 segments. Also absolute energy gain tuning is not yet made at this stage.

We then plotted the CTI-corrected data for the 4 segments (segments A, B, C, and D) of each XIS set, and the results are shown in figures 14, 15, and 16.

We found significant gain differences from segment to segment in each XIS set and from XIS CCD to CCD in the segment-averaged energy. The absolute gains for the segments including the calibration sources were fine-tuned to the energy of the calibration lines ( $K\alpha$  and  $K\beta$  lines of Mn I). The gains of the other segments were adjusted to match the center energies of the 3 K-shell lines (S XV, Fe I, and Fe XXV) to those of the fine-tuned energies of the calibration segments. The results are given in figures 17, 18, and 19. Note that the vertical axis scales are finer than those of figures 8–16. We see the energy variations from XIS CCD to CCD and/or from segment to segment become smaller than those of the non-correction in both the S and Fe  $K\alpha$  lines.

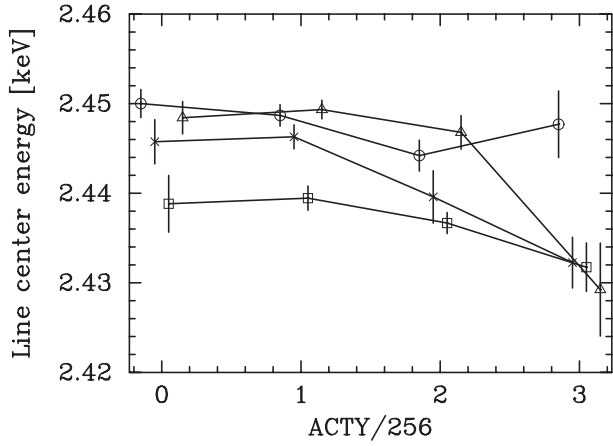


**Fig. 8.** The center energy of S XV  $K\alpha$ . In the 4 regions of IA divided along the ACTY axis for each XIS set. Circles, crosses, squares, and triangles represent line center energy obtained with XIS 0, XIS 1, XIS 2, and XIS 3, respectively.

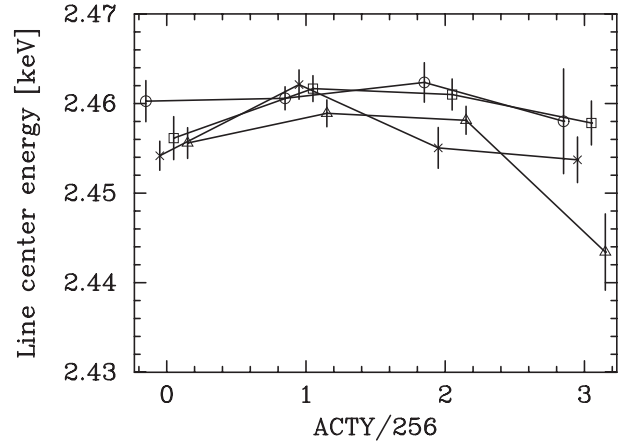


**Fig. 11.** Same as figure 8, but after the CTI correction.

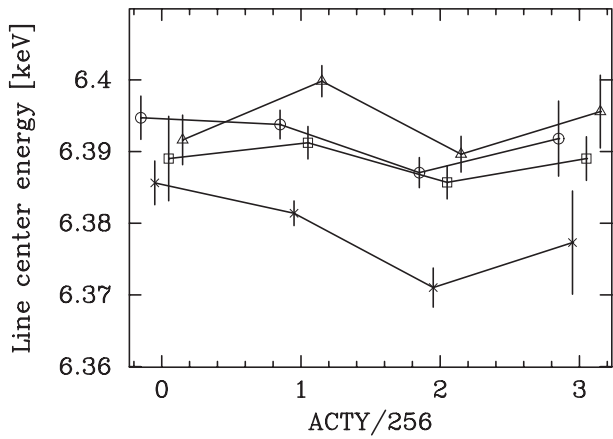


**Fig. 9.** Same as figure 8, but for the Fe I  $K\alpha$  line.

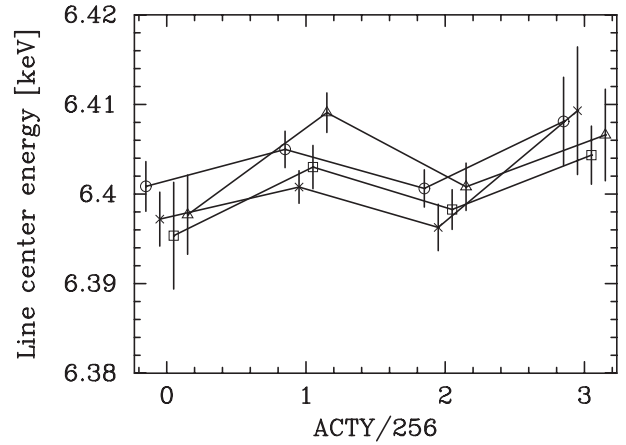


**Fig. 12.** Same as figure 11, but for the Fe I  $K\alpha$  line.

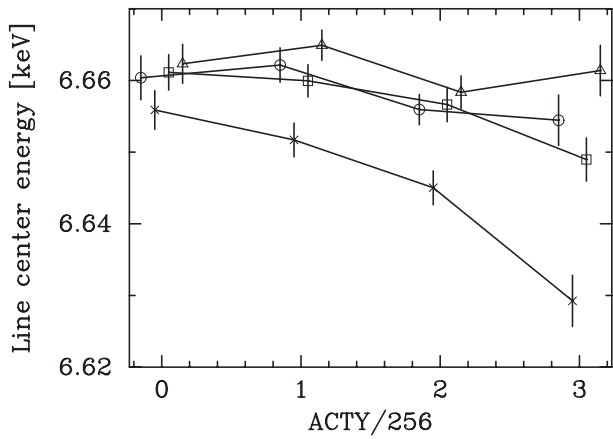


**Fig. 10.** Same as figure 8, but for the of Fe XXV  $K\alpha$  line.

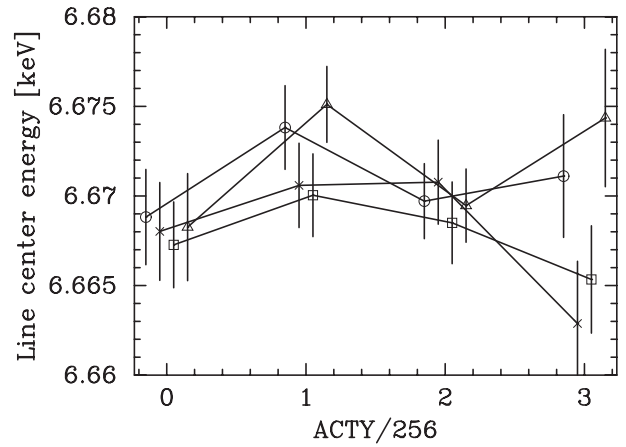


**Fig. 13.** Same as figure 11, but for the Fe XXV  $K\alpha$  line.

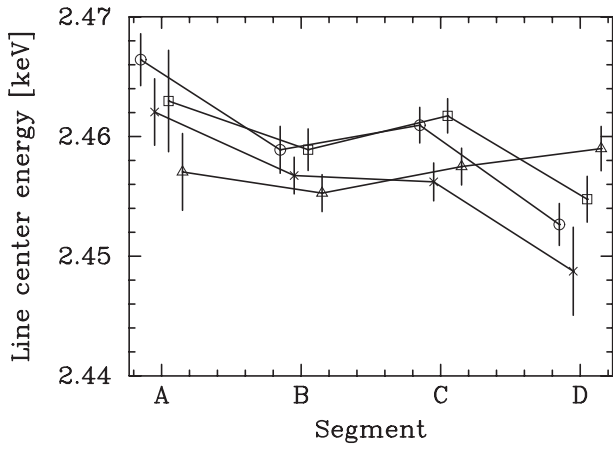


Fig. 14. The center energy of SXV K $\alpha$  after the CTI correction in the 4 segments of each XIS set. The symbols are the same as figure 8.

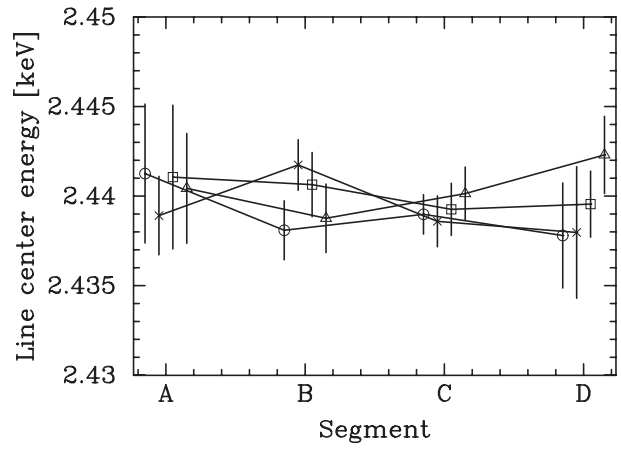


Fig. 17. The same as figure 14, but after the gain correction among the each segment. The symbols are the same as figure 8.

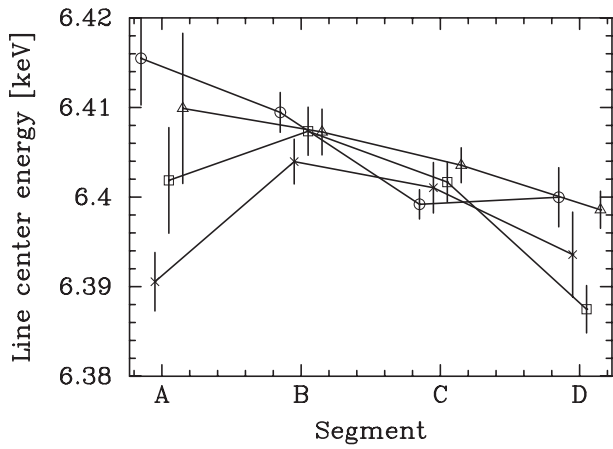


Fig. 15. Same as figure 14, but for the of Fe I K $\alpha$  line.

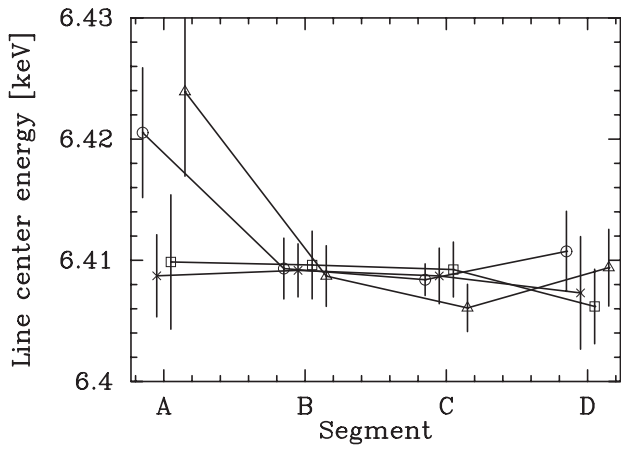


Fig. 18. Same as figure 17, but for the Fe I K $\alpha$  line.

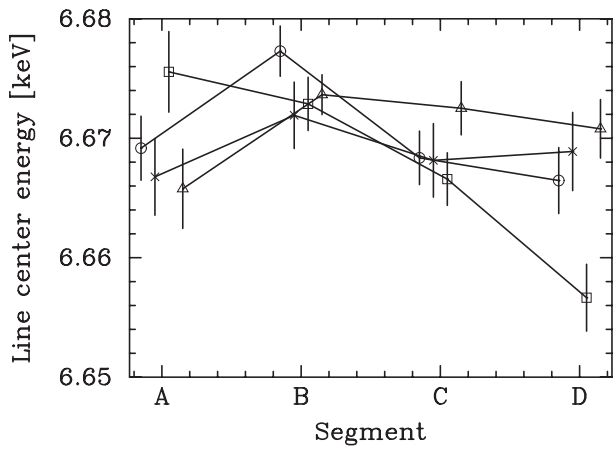


Fig. 16. Same as figure 14, but for the of Fe XXV K $\alpha$  line.

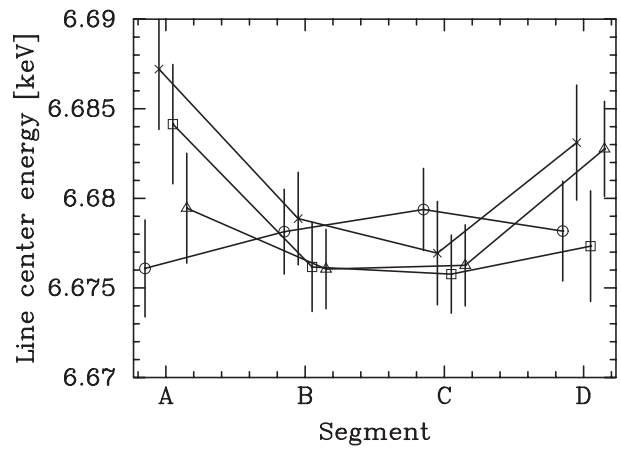


Fig. 19. Same as figure 17, but for the Fe XXV K $\alpha$  line.

## References

- Aharonian, F., et al. 2006, *Nature*, 439, 695
- Anders, E., & Grevesse, N. 1989, *Geochim. Cosmochim. Acta*, 53, 197
- Beiersdorfer, P. 2003, *ARA&A*, 41, 343
- Beiersdorfer, P., et al. 1992, *Phys. Rev. A*, 46, 3812
- Beiersdorfer, P., et al. 1993, *ApJ*, 409, 846
- Beiersdorfer, P., et al. 2005, *Phys. Rev. A*, 72, 032725
- Kaastra, J. S., & Mewe, R. 1993, *A&AS*, 97, 443
- Kosack, K., et al. 2004, *ApJ*, 608, L97
- Koyama, K., et al. 2007a, *PASJ*, 59, S23
- Koyama, K., et al. 2007b, *PASJ*, 59, S237
- Koyama, K., Awaki, H., Kunieda, H., Takano, S., Tawara, Y., Yamauchi, S., Hatsukade, I., & Nagase, F. 1989, *Nature*, 339, 603
- Koyama, K., Maeda, Y., Sonobe, T., Takeshima, T., Tanaka, Y., & Yamauchi, S. 1996, *PASJ*, 48, 249
- Maeda, Y., et al. 2002, *ApJ*, 570, 671
- Mitsuda, K., et al. 2007, *PASJ*, 59, S1
- Morris, M., et al. 2003, in *Proc. the Galactic Center Workshop 2003 — The central 300 parsecs of the Milky Way*, *Astron. Nachr. Suppl.*, 324, 167
- Muno, M. P., et al. 2003, *ApJ*, 589, 225
- Muno, M. P., et al. 2004, *ApJ*, 613, 326
- Murakami, H., Koyama, K., & Maeda, Y. 2001, *ApJ*, 558, 687
- Murakami, H., Koyama, K., Sakano, M., Tsujimoto, M., & Maeda, Y. 2000, *ApJ*, 534, 283
- Orlando, S., Olson, R. E., & Beiersdorfer, P. 2006, *Phys. Rev. A*, 73, 022723
- Park, S., et al. 2005, *ApJ*, 631, 964
- Park, S., Muno, M. P., Baganoff, F. K., Maeda, Y., Morris, M., Howard, C., Bautz, M. W., & Garmire, G. P. 2004, *ApJ*, 603, 548
- Perez, J. A., Olson, R. E., & Beiersdorfer, P. 2001, *J. Phys. B*, 34, 3063
- Predehl, P., Costantini, E., Hasinger, G., & Tanaka, Y. 2003, *Astron. Nachr.*, 324, 73
- Sakano, M., Koyama, K., Murakami, H., Maeda, Y., & Yamauchi, S. 2002, *ApJS*, 138, 19
- Sakano, M., Warwick, R. S., Decourchelle, A., & Predehl, P. 2004, *MNRAS*, 350, 129
- Senda, A., Murakami, H., & Koyama, K. 2002, *ApJ*, 565, 1017
- Serlemitsos, P., et al. 2007, *PASJ*, 59, S9
- Takahashi, T., et al. 2007, *PASJ*, 59, S35
- Tanaka, Y. 2002, *A&A*, 382, 1052
- Tanaka, Y., Koyama, K., Maeda, Y., & Sonobe, T. 2000, *PASJ*, 52, L25
- Tsuchiya, K., et al. 2004, *ApJ*, 606, L115
- Valinia, A., Tatischeff, V., Arnaud, K., Ebisawa, K., & Ramaty, R. 2000, *ApJ*, 543, 733
- Wargelin, B. J., Beiersdorfer, P., Neill, P. A., Olson, R. E., & Scofield, J. H. 2005, *ApJ*, 634, 687
- Yamauchi, S., Kawada, M., Koyama, K., Kunieda, H., Tawara, Y., & Hatsukade, I. 1990, *ApJ*, 365, 532

